Ku-Band Suspended Meshed Patch Antenna Integrated with Solar Cells for Remote Area Applications

Farhat Nashad[1, *], Stephen Foti[1], David Smith[1], Michael Elsdon[1], and Okan Yurduseven[2]

Abstract—A new structure design of a dual-band suspended microstrip meshed patch antenna integrated with a polycrystalline silicon solar cell for Ku-band satellite applications is proposed and presented. This antenna element is a basic building block for a Ku-band meshed array antenna used for two-way satellite internet and TV applications at rural and remote locations. The antenna covers the operating frequency range from 11.7 GHz to 12.22 GHz downlink band and from 14.0 GHz to 14.5 GHz uplink band allocated by the ITU to the Regions 1 and 2. While achieving 500 MHz bandwidth across each band, fully covering the Ku-band uplink and downlink frequency bands, the antenna offers a single element gain of 6.05 dBi in the downlink band and 7.61 dBi in the uplink band. The antenna has been fabricated and measured, and good agreement is achieved between the experimental and simulated results. In addition, a good compromise between RF performance and optical transparency is obtained. The overall visible light transmission is found to be approximately 87%. A compact low-profile antenna element is also achieved.

1. INTRODUCTION

Wireless communications have evolved rapidly over the past years, and demands on communications services require higher data rates over long distances [1]. Today's satellite communications have advantages over other communication technologies for remote applications, and provide good solutions, such as constant connectivity, redundancy and back-up service for remote locations. In a number of applications in places where the electric power grid is not easily obtainable, communication systems with uninterruptible power source capabilities are required to provide long-term and continuous communication services. Photovoltaic (PV) solar cell panels can serve as a viable power source to satellite communication terminals at remote areas. Such as; remote homes, caravans, and also at remote industrial locations, for instance Supervisory Control and Data acquisition (SCADA) of remote fixed sites, for gas and oil protection monitoring points. Moreover, for different security pipelines cathodic substations of remote sites [1, 2]. In any of the previous applications, the collected data information is transmitted or received from/to satellite via two-way wireless communication systems. In these systems the antenna is a key component and recent years have witnessed growing interest and increasing need to provide a small size, lightweight, high gain broadband antennas for high performance wireless communication systems [2, 3]. In such remote applications, the microwave antennas and solar PV cells ideally work independently of each other, in order to avoid any electromagnetic or thermal interference. This stand-alone arrangement has an effect on the size, weight and surface area that has to be large enough, hence, costly [4]. The PV solar panels, in addition to their function as a power

source, can also be integrated with microwave antennas [5]. This integration of microwave antennas and PV technology on the same surface has led to the development of self-powered integrated systems that can be configured by a variety of design techniques, and can help to reduce the weight and peripheral expense of the system. Hence, this represents a cost-effective system due to the possibility of integrated production [6, 7]. Furthermore, this technology could be used for satellite and terrestrial systems. In relevant studies, several researches have been carried out on the integration of microwave antennas and solar PV cells [8, 9]. First combined photovoltaic solar printed patch antenna was proposed by [10], then the integrated solar cells with antennas have been developed recently with dramatic success, in order to achieve a good antenna performance and a compromise between RF performance and transparency as in [11]. However, the design presented in [11] exhibits a bi-directional radiation pattern due to the truncated ground plane and therefore is not suitable for SATCOM applications. Analyzing the full-integration topologies presented in [10, 12–17] most studies have focused on the combination of solar PV cells and antennas operating in relatively low frequency bands and exhibiting narrow bandwidths.

In this paper, a dual Ku-band suspended meshed patch antenna is presented. The photovoltaic antenna uses a suspended integration topology and has an optically transparent substrate integrated with solar cells. The developed antenna serves as a basic element for a Ku-band transparent array antenna with direct-coupling feeding to achieve high performance for long distance communications, such as ground-to-space satellite communications in order to increase data rate. This antenna can be specifically used for Fixed-Satellite-Services (FSS) operating over the frequency range from 11.7 GHz to 12.22 GHz (downlink) and 14.0 GHz to 14.5 GHz (uplink) bands that are allocated by the International Telecommunication Union (ITU) to the Regions 1 and 2.

2. MESHED PATCH ANTENNA DESIGN AND FABRICATION

The proposed suspended meshed patch antenna with dimensions of 6.0 mm × 6.0 mm × 35 μm together with the feeding structure is designed using CST Microwave Studio as shown in Fig. 1(a). The antenna was developed on a transparent Plexiglas substrate with thickness of 1.5 mm and dielectric constant (ε_r) of 2.59, with a meshed copper ground plane on the substrate lower side. The patch and ground plane have track widths (w_t) of 0.5 mm. The patch is fed by a microstrip line through a quarter-wave transformer for improving the impedance matching. In this design, the overall patch dimensions were determined based on the transmission line model for designing a solid patch to operate at the desired frequency of 11.95 GHz [18]. The meshed ground plane has been designed with wide slots in dimensions in order to improve the overall transparency of the antenna while maintaining the RF performance. The suspended meshed patch has four square slots and is suspended with four transparent stands in the corners above the radiating element, with an air gap of 2.0 mm, as shown in Fig. 1(b). The antenna is located above a poly-Si solar cell with thickness of 0.2 mm. The solar cell is encapsulated in between a Perspex glass layer on the top and rear contact an aluminum layer covering the back of the
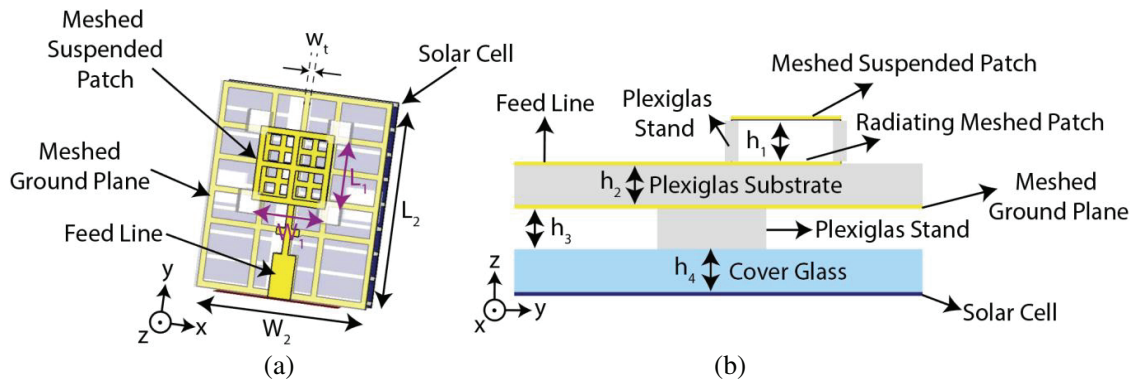

Figure 1. Suspended meshed patch antenna integrated with solar cell: (a) overall view in CST microwave studio, (b) side view. Dimensions: $W_1 = 6$ mm, $W_2 = 15$ mm, $w_t = 0.5$ mm, $L_1 = 6$ mm, $L_2 = 18$ mm, $h_1 = 2$ mm, $h_2 = 1.5$ mm, $h_3 = 2$ mm, $h_4 = 3$ mm.

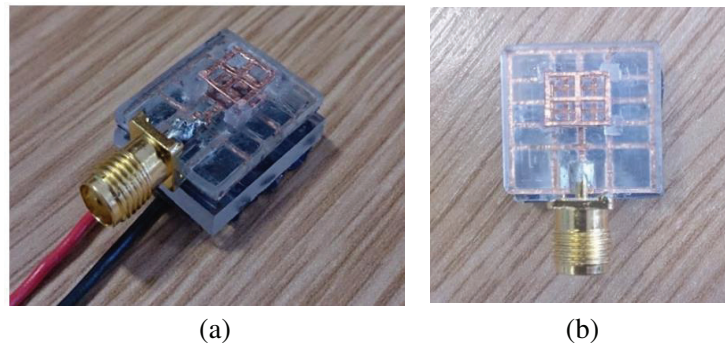(a)   (b)

Figure 2. A photograph of fabricated proposed meshed patch antenna: (a) perspective side view (b) front view.

solar cell It has the same dimensions of the antenna substrate with an air gap of 2.0 mm in between. The microstrip fed-line suspended meshed patch antenna was fabricated and connected to 50 Ω-SMA connector and tested using a vector network analyzer (Agilent N5230A). Photographs of the fabricated proposed design antenna integrated with solar cells are shown in Fig. 2. In this presented design, a standard SMA connector (straight PCB mount type) was used.

3. SIMULATION AND MEASUREMENT RESULTS

The simulated and measured reflection coefficient ($|S_{11}|$) patterns of the antenna are illustrated in Fig. 3. It is evident in Fig. 3 that there are two resonances each providing broad bandwidth according to the simulation and practical results. The simulated results were carried out using CST Microwave Studio and show that S_{11} response of better than -10 dB is achievable over 500 MHz in both the downlink and uplink bands. The measured S_{11} shows that the fabricated proposed antenna resonates close to the desired frequencies. There is a small difference between the simulated and measured uplink-band resonant frequencies. This is attributed to the hand-constructed fabrication process and the caused imperfections in the resulting dimensions. Clearly, it is extremely difficult to cut the mesh cells by hand and chemical etching would improve the fabrication accuracy. Otherwise, good agreement between the simulation and practical measurement has been achieved.
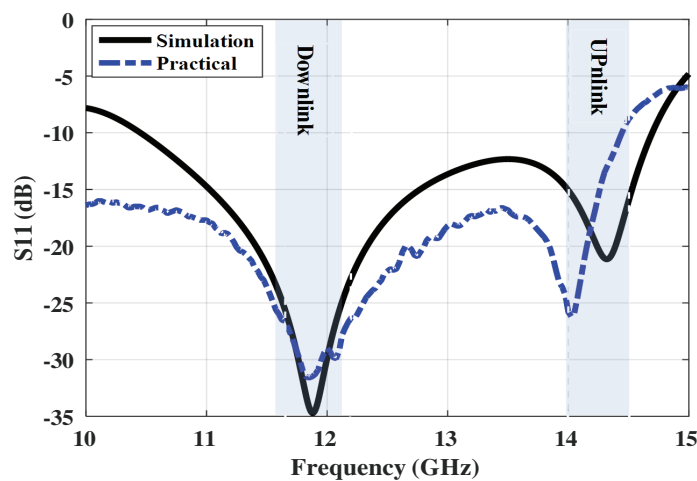

Figure 3. Simulated and practical results of S_{11}-parameters.

3.1. Effect of Variation of the Grid Line Width on the S_{11} Antenna Performance

As mentioned earlier, the line width for the meshed patch is $w_t = 0.5$ mm. Following the analysis of the S_{11} response of the antenna, the effect of varying the grid line width on the antenna performance is studied. Reducing the line width has an advantage of improving the optical transparency of the antenna, ensuring optimum photovoltaic characteristics. However, it can significantly affect the RF performance, and therefore, a careful analysis must be carried out to find the optimum line width as shown in Fig. 4.
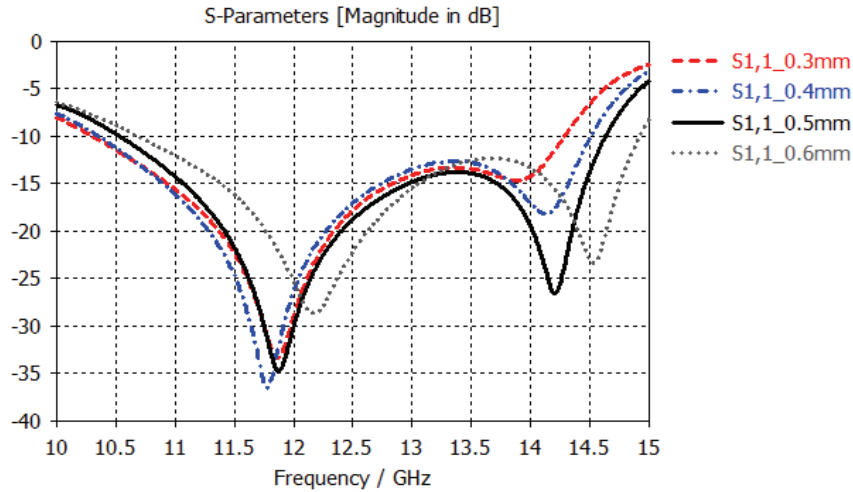

Figure 4. Effect of variation of the grid line width on the S_{11}-parameter.

The effect of decreasing the vertical and horizontal meshed line widths can be seen in Fig. 4. Analyzing Fig. 4, a significant change in the S_{11} response and degradation in the uplink band performance is noted when the line width is reduced below 0.5 mm. It has been observed that as the transparency of the meshed patch is increased from 87% to 95% due to reducing the grid line width from 0.5 mm to 0.3 mm, the performance is decreased. When the width is increased above 0.5 mm to 0.6 mm, both resonances of S_{11}-response are shifted to higher frequency. This is due to decreasing apertures dimensions, hence decreasing the electrical length of the current path. As a result of this study, the optimum line width for the meshed patch is found to be $w_t = 0.5$ mm, and the antenna becomes ineffective when the line width is shorter than 0.3 mm, $w_t \leq 0.3$ mm.

3.2. Effect of Solar Cell on the Meshed Antenna Performance

In order to discuss the effect of solar integration on the antenna performance, the proposed microstrip meshed patch antenna design with and without integrated solar cell was simulated using CST Microwave Studio and is illustrated in Fig. 5.

A comparison is made in Fig. 6, between the simulated S_{11}-responses of two cases of the proposed suspended transparent solar patch antenna with and without the solar cell.

Analyzing Fig. 6, it is evident that the presence of the solar cell affects the S_{11}-response of the antenna, and therefore, the design parameters were optimized in the presence of the solar cell. In Fig. 6, the downlink resonance frequency is shifted by 650 MHz from the intended design frequency of 11.95 GHz to 11.3 GHz while the uplink resonance frequency is shifted by 200 MHz from 14.45 GHz to 14.25 GHz. The simulated radiation patterns of the antenna with and without the solar cell are illustrated in Fig. 7.

As can be seen in Fig. 7(a), the downlink radiation characteristics of the antenna in the H-plane with and without solar cell are nearly identical in gain and radiation patterns. In Figs. 7(b), (c) and (d) slight differences are observed with the antenna without the integrated solar cell exhibiting a back-lobe radiation below -10 dB. It is found that by using the meshing technique, the antenna becomes transparent and the bandwidth is increased. However, it has a degraded front to back ratio (FBR),
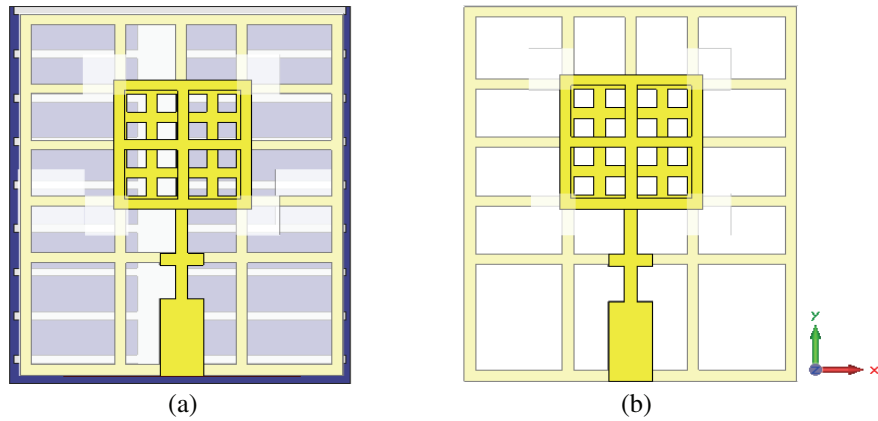
(a)   (b)

Figure 5. Proposed suspended meshed patch antenna (a) with solar cell (b) without solar cell and cover glass (with only meshed ground plane).
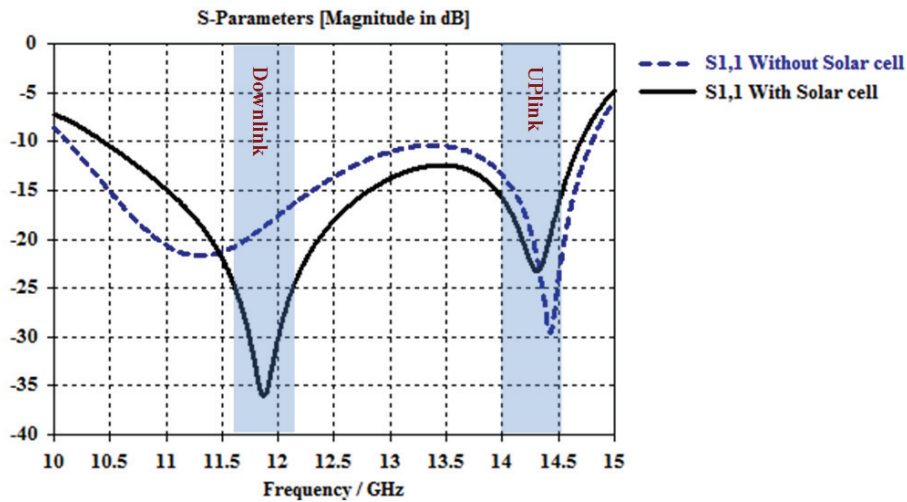

Figure 6. Simulated S_{11}-parameters of suspended meshed antenna with and without solar cell.

due to the partial decline in the ground plane conductivity, thus, reducing the gain from 7.885 dBi to 6.69 dBi in the H-plane (Fig. 7(b), dashed line) and from 8.05 dBi to 6.79 dBi in the E-plane (Fig. 7(d)) at 14.25 GHz uplink (solid and dashed lines), respectively. In addition, it can be noticed in Fig. 7(d) that the antenna has a pattern similar to monopole radiation pattern in the uplink E-plane without solar cell (dashed line). Alternative solutions can be utilized in order to improve FBR, in the case of solar antenna integration; the solar cells can play the role of an additional ground plane, thus, kill the back-lobe radiation, which is reduced from $0 \sim -8$ dB to about -20 dB, and hence improving the directivity and the gain, as shown in Figs. 7(b) and 7(d) (solid lines).

3.3. Impedance Characteristics

To study the impedance characteristics of the proposed antenna, the real and imaginary results are plotted in Figs. 8(a) and (b).

It can be seen from Fig. 8(a) that the real parts of the simulated and measured input impedance patterns of the antenna are in good agreement. The simulated real parts for both the downlink and uplink bands are very close to 50 Ω source impedance, and the imaginary part shown in Fig. 8(b) is close to zero, indicating good impedance matching at both resonant frequencies. For the measured
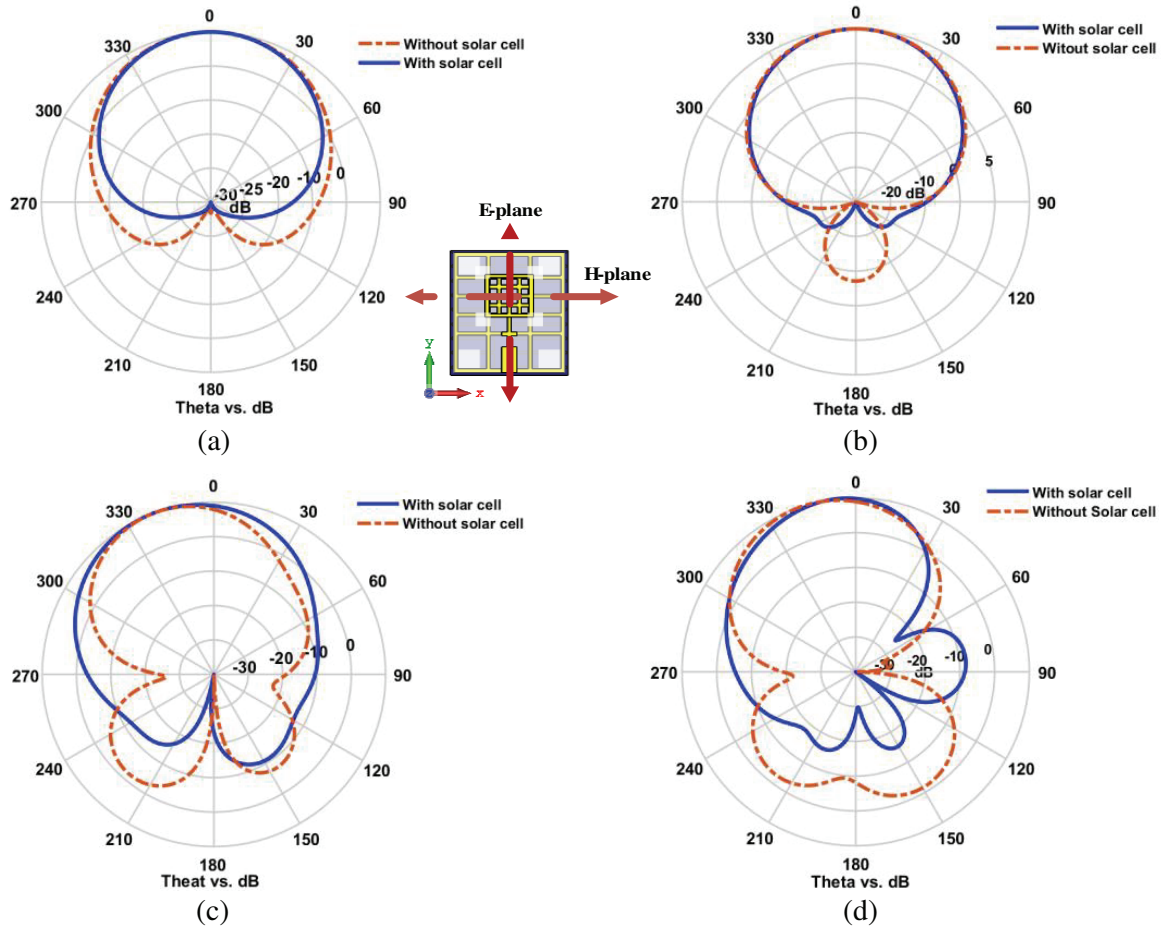
Figure 7. Simulated radiation patterns of the meshed antenna with and without solar cell: (a) H-plane downlink/with and without solar cells (b) H-plane uplink/with and without the solar cells, (c) E-plane downlink/with and without solar cells, (d) E-plane uplink/with and without the solar cells.
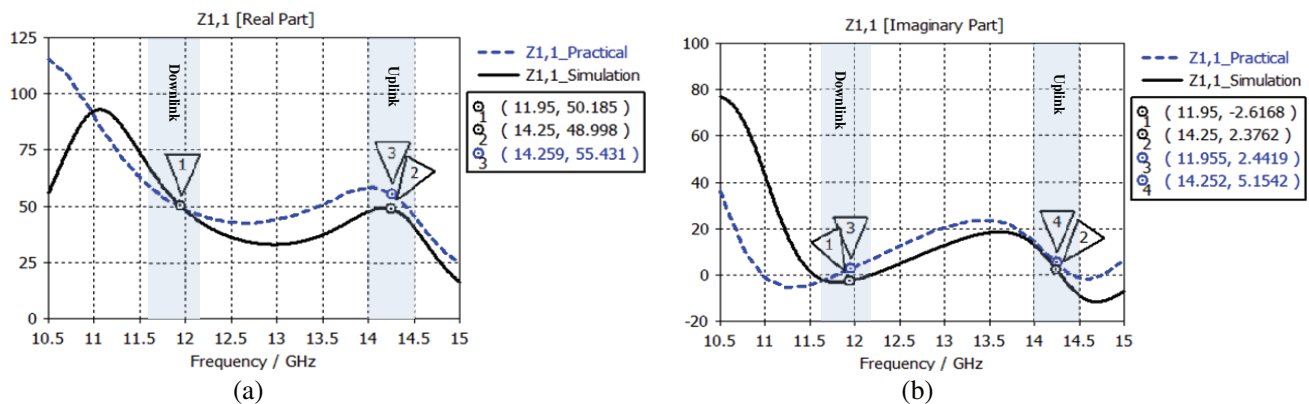
Figure 8. Z-parameters (a) real, and (b) imaginary parts of the meshed patch antenna.

impedance pattern at the uplink band, the real part has a slightly higher real impedance value than the simulated pattern with the difference being about $6.4\,\Omega$. The imaginary part values are close to zero at the desired resonance frequency for both bands, oscillating around $2.6\,\Omega$. There is a fairly good agreement between the simulated and experimental impedance patterns.

3.4. Current Distribution

Figure 9, shows the simulated surface current distribution of the proposed meshed antenna at 11.95 GHz and 14.25 GHz downlink and uplink bands respectively. The surface current flows through the feed line towards the multi-slots radiating element, and the current is distributed into the vertical (y-axis) and horizontal (x-axis) directions along the slot edges. The current density induces an E-field across the slots and therefore, contributes to radiation and creates resonance frequency modes. As can also be seen in Fig. 9, the highest current intensity is focused on the edges towards the x-direction and is reduced at the centre of the patch. The loading slots effect the current flow paths and cause the current to travel a longer distance around the slots, which effectively increases the size of the patch antenna electrically and reduces the resonance of the TM_{01} mode down towards the fundamental frequency. This explains the reason that the meshed square patch is miniaturized.
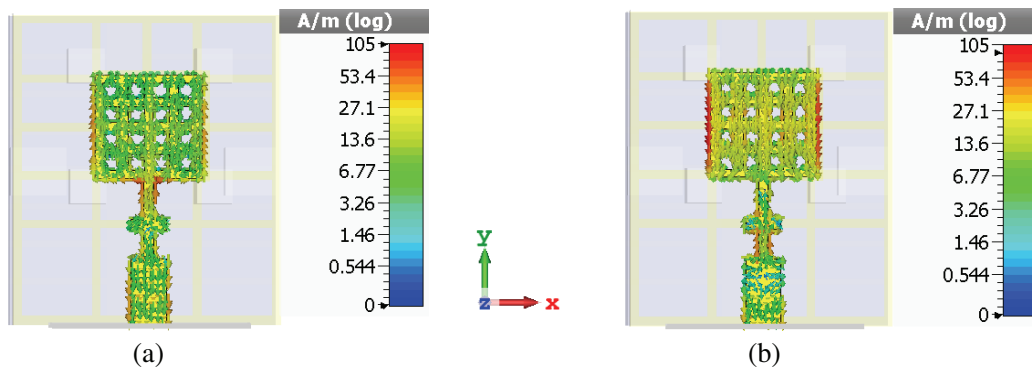

Figure 9. Current distribution across the suspended meshed patch at (a) 11.95 GHz, (b) 14.25 GHz bands.

3.5. Radiation Pattern

The simulated and measured E-plane and H-plane far-field radiation patterns for downlink and up-link bands are shown in Figs. 10(a) and (b). The measurements were carried out in an anechoic chamber, and a standard horn antenna with known gain of 20 dBi was used as a reference antenna. The performance parameters at the center frequencies of both bands are summarized in Table 1.

It can be noticed in Fig. 10 that there is good agreement between the simulated and measured far-field patterns in the H-plane (x-z plane). The discrepancy in the E-plane (y-z plane) can be attributed to a number of reasons. A very important factor can be understood by analyzing the surface current distributions presented in Fig. 9. It can be seen in Fig. 9 that the surface current flows dominantly in the y-direction (as opposed to x-direction). As a result, any differences in the meshed wire configuration between the simulation and experimental models of the antenna (including the position, width and flatness of the copper tracks of the meshed patch) can cause such differences between the simulated and experimental E-plane patterns as opposed to H-plane patterns exhibiting superior agreement.

It is noted that good overall antenna efficiency and high power gains are observed at both resonance frequency bands, confirming that the proposed antenna works properly at both desired bands. The antenna exhibits simulated realized gains of 6.75 dBi for downlink and 8.05 dBi uplink bands with 3 dB beam widths of 90.7° and 74.°, respectively. The obtained radiation efficiency is −0.60 dB (87.1%) for the downlink band and −0.58 dB (87.5%). The total efficiency for the desired bands are −0.82 dB (82.6%) and −0.72 dB (84.5%) respectively while the measured downlink and uplink gains are reported to be 6.05 dBi and 7.61 dBi. The differences between the simulated and experimental results can be attributed to the imperfections in the construction process of the antenna and fabrication tolerances. It was also noticed that the uplink power gain is higher than that at the downlink band. This is due to the narrower beam-width at uplink band, and 14.25 GHz the wavelength is smaller than the downlink, resulting in an electrically larger aperture size in the uplink band. The results also show that the
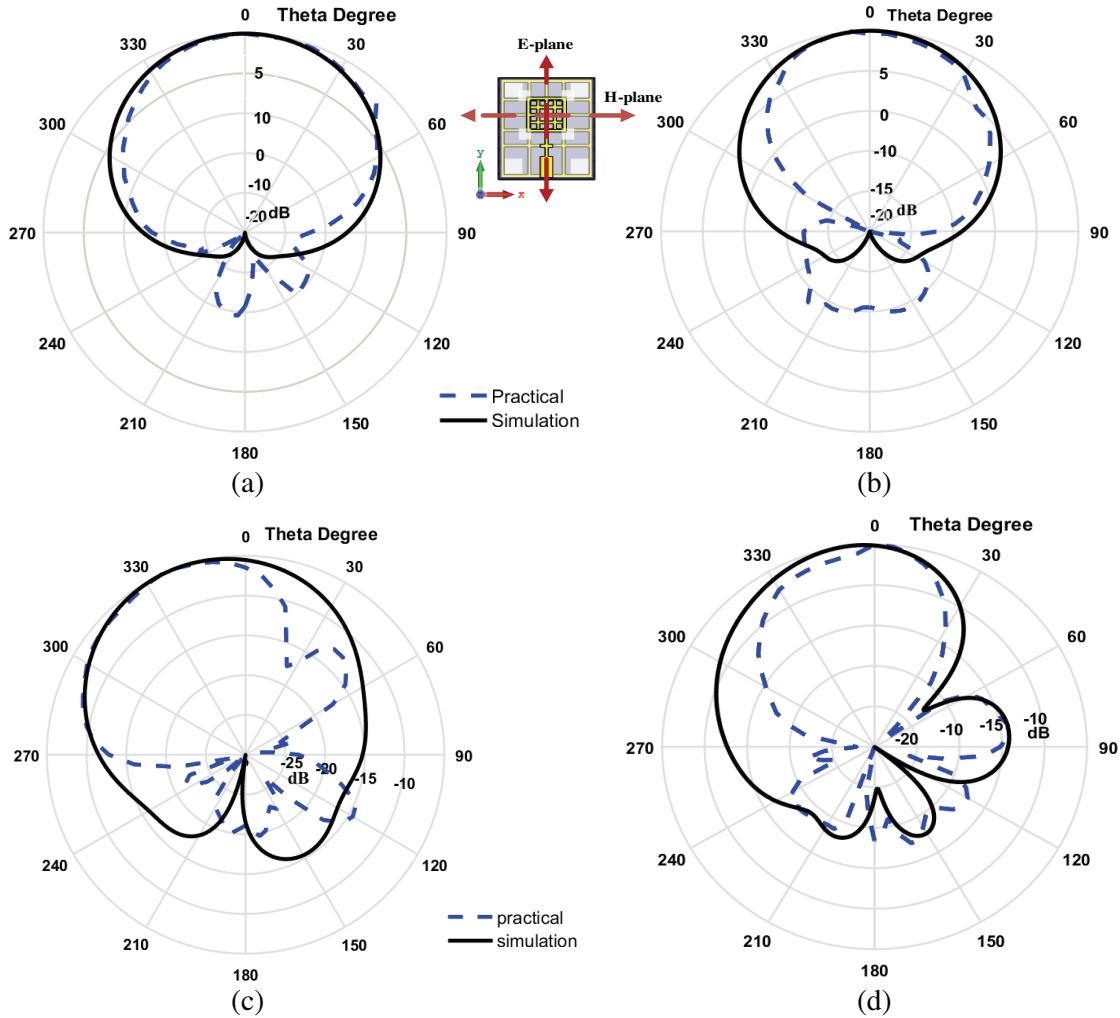
Figure 10. Simulated and measured results of far-field radiation patterns: (a) *H*-plane downlink, (b) *H*-plane uplink, (c) *E*-plane downlink, (d) *E*-plane uplink for suspended transparent patch antenna.

Table 1. Performance results for the proposed antenna over the uplink and downlink frequency bands.

Antenna Parameters	Centre frequency (GHz)	Impedance Bandwidth (MHz)	Realized Gain (dBi)		Beam width (3dB)	Radiation Efficiency (dB)	Total Efficiency (dB)
			Simulated	measured			
Downlink band	11.95	> 500	6.75	6.055	90°.7	-0.60 (87.1%)	-0.82 (82.6%)
Uplink band	14.25	> 500	8.05	7.61	74.0°	-0.58 (87.5%)	-0.72 (84.5%)

achieved impedance bandwidth in each portion was 500 MHz. A VSWR of less than or equal to 1.1 was obtained at both uplink and downlink frequency bands. The overall optical transparency of the meshed radiating element has been calculated as 87.0%, based on Equation (1) given below:

$$\text{Transparency (\%)} = 100 * \frac{\text{Antenna Transparent Area}}{\text{Antenna Solid Area}} \tag{1}$$

4. SOLAR CELL ELECTRICAL CHARACTERISTICS

The solar cell electrical characteristics, such as the open-circuit voltage (V_{oc}) and short-circuit current (I_{sc}), were measured with and without the integrated suspended meshed patch antenna element as shown in Fig. 9. In order to compare the effect of the solar antenna integration topology on the transparency and illumination efficiency operation of the solar cell, the antenna's transparent substrate and the Poly-Si solar cell have the same dimensions, 18.0 mm × 15.0 mm. The simulation was carried out by using a Flood Light Solar Simulator in an electrical power workshop, with measured light intensity of $450 \, \text{W/m}^2$, and the light was focused on the solar cell, with the cell electrical output wires being connected to an Ampere-Volt-Ohm (AVO) meter in order to measure the generated output DC voltage and current. For non-integrated antenna element, V_{oc} and I_{sc} values were measured to be $V_{oc} = 69 \, \text{mV}$ and $I_{sc} = 0.18 \, \text{mA}$, resulting in a DC power output of $12.42 \, \mu\text{W}$. In contrast, when the meshed antenna element is placed above the solar cell, the observed output values were slightly decreased to $V_{oc} = 62 \, \text{mV}$ and $I_{sc} = 0.165 \, \text{mA}$, respectively, resulting in a DC power output of $10.23 \, \mu\text{W}$. The use of the radiating meshed antenna element has yielded little decrease in output DC power of $2.19 \, \mu\text{W}$ at normal incidence, compared to the DC solar power without any antenna integrated above, and this is reasonable and acceptable.

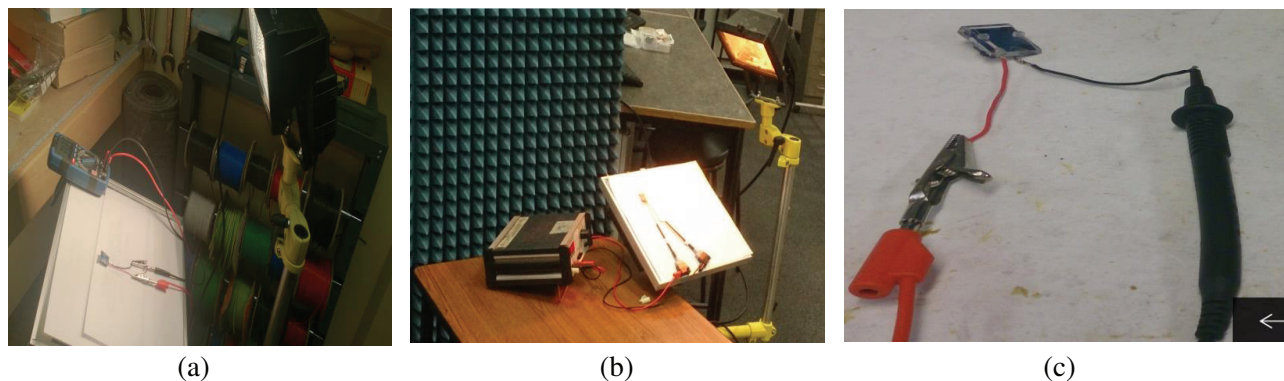(a)   (b)   (c)

Figure 11. Polycrystalline solar cell DC characteristics measurement; (a) flood Light Solar Simulator (normal incidence) (b) from oblique angle (c) without any antenna integrated above.

For practical applications, the solar illumination angle does not remain constant. To investigate the effect of changing the illumination angle on the solar cell performance, additional measurements were carried out with different tilt angles as shown in Fig. 11(b). It was observed that the output values of V_{oc} and I_{sc} are reduced to $V_{oc} = 57 \, \text{mV}$ and $I_{sc} = 0.12 \, \text{mA}$, resulting in a DC power output of $6.84 \, \mu\text{W}$. This is due to the impact of optical shading at oblique illumination angles caused by the non-direct photovoltaic illumination.

5. CONCLUSION

In this paper, the design of a dual-band suspended transparent meshed patch antenna for use in Ku-band satellite communication systems has been proposed and demonstrated. This new design provides a building block of an integrated communication system for remote area satellite applications. The antenna covers the frequency bands ranging from 11.7 GHz to 12.22 GHz (downlink) and 14.0 GHz to 14.5 GHz (uplink) allocated by the ITU to Regions 1 and 2, with instantaneous bandwidths of 500 MHz obtained in each portion for broadband two-way satellite internet and TV applications. The results have shown no significant degradation in overall antenna performance while a compromise has been achieved between RF performance and overall transparency, which has yielded realized element gains of 6.05 dBi and 7.61 dBi, for downlink and uplink bands, respectively. The overall optical transparency of the antenna has been found to be approximately of 87%. The developed antenna is compact and in low profile.

REFERENCES

1. Vaccaro, S., J. R. Mosig, and P. de Maagt, "Two advanced solar antenna "SOLANT" designs for satellite and terrestrial communications," *IEEE Transactions on Antennas and Propagation*, Vol. 51, No. 8, 2028–2034, Aug. 2003.

2. Lee, R., E. Clark, D. Wilt, A. Pal, F. Miranda, C. Mueller, et al., "Integrated solar cell array antenna for satellite and terrestrial communications," *2005 IEEE Antennas and Propagation Society International Symposium*, 231–234, 2005.

3. Maharaja, M. and C. Kalaiselvan, "Integration of antennas and solar cells for satellite and terrestrial communication," *International Journal of Scientific and Research Publications*, Vol. 3, 2013.

4. Dreyer, P., M. Morales-Masis, S. Nicolay, C. Ballif, and J. Perruisseau-Carrier, "Copper and transparent-conductor reflectarray elements on thin-film solar cell panels," *IEEE Transactions on Antennas and Propagation*, Vol. 62, 3813–3818, 2014.

5. Bendel, C., J. Kirchhof, and N. Henze, "Application of photovoltaic solar cells in planar antenna structures," *Proceedings of 3rd World Conference on Photovoltaic Energy Conversion*, 220–223, 2003.

6. Baccouch, C., D. Bouchouicha, H. Sakli, and T. Aguili, "Patch antenna based on a photovoltaic cell with a dual resonance frequency," *Advanced Electromagnetics*, Vol. 5, No. 3, 42–49, Nov. 11, 2016.

7. Roo-Ons, M. J., S. V. Shynu, M. J. Ammann, S. J. McCormack, and B. Norton, "Transparent patch antenna on a-Si thin-film glass solar module," *Electronics Letters*, Vol. 47, No. 2, 85–86, Jan. 2011.

8. Shynu, S. V., M. J. Ons, P. McEvoy, M. J. Ammann, S. J. McCormack, and B. Norton, "Integration of microstrip patch antenna with polycrystalline silicon solar cell," *IEEE Transactions on Antennas and Propagation*, Vol. 57, No. 12, 3969–3972, Dec. 2009.

9. Shynu, S., M. R. Ons, M. Ammann, S. Gallagher, and B. Norton, "Inset-fed microstrip patch antenna with integrated polycrystalline photovoltaic solar cell," *The Second European Conference on Antennas and Propagation, 2007, EuCAP 2007*, 1–4, 2007.

10. Tanaka, M., Y. Suzuki, K. Araki, and R. Suzuki, "Microstrip antenna with solar cells for microsatellites," *Electronics Letters*, Vol. 31, 5–6, 1995.

11. Yurduseven, O., D. Smith, and M. Elsdon, "A transparent meshed solar monopole antenna for UWB applications," *2014 8th European Conference on Antennas and Propagation (EuCAP)*, 2145–2149, 2014.

12. Fawole, O. and R. Baktur, "Multifunction solar panel antenna for cube satellites," *2012 IEEE Antennas and Propagation Society International Symposium (APSURSI)*, 1–2, 2012.

13. Yurduseven, O., D. Smith, N. Pearsall, I. Forbes, and D. Johnston, "A meshed multiband solar patch array antenna," *Antennas and Propagation Conference (LAPC), 2012 Loughborough*, 1–5, 2012.

14. Elsdon, M., O. Yurduseven, and X. Dai, "Wideband metamaterial solar cell antenna for 5 GHz Wi-Fi communication," *Progress In Electromagnetics Research C*, Vol. 71, 123–131, 2017.

15. O'Conchubhair, O., P. McEvoy, and M. J. Ammann, "Dye-sensitized solar cell antenna," *IEEE Antennas and Wireless Propagation Letters*, Vol. 16, 352–355, 2017.

16. Turpin, T. W. and R. Baktur, "Meshed patch antennas integrated on solar cells," *IEEE Antennas and Wireless Propagation Letters*, Vol. 8, 693–696, 2009.

17. Yasin, T. and R. Baktur, "Circularly polarized meshed patch antenna for small satellite application," *IEEE Antennas and Wireless Propagation Letters*, Vol. 12, 1057–1060, 2013.

18. Balanis, C., *Antenna Theory Analysis and Design*, 3rd Edition, John Wiley & Sons, Inc., Publication, 2005.